The SPT Telescope: A Brief Overview of Design of Past Surveys and Analysis of the future Design of SPT-SLIM

by

Raymundo Basilio Torrez

A Thesis Submitted to the Faculty of the

DEPARTMENT OF OPTICS

In Partial Fulfillment of the Requirements

For the Degree of

MASTER OF SCIENCE

In the Graduate College

THE UNIVERSITY OF ARIZONA

2024

THE UNIVERSITY OF ARIZONA
GRADUATE COLLEGE

As members of the Master's Committee, we certify that we have read the thesis prepared by *[Enter Student Name –remove brackets and italics after entering information]*, titled *[Enter Thesis Title]* and recommend that it be accepted as fulfilling the dissertation requirement for the Master's Degree.

____ Date: ____________
[Committee Chair Name]

____ Date: ____________
[Committee Member Name]

____ Date: ____________
[Committee Member Name]

Final approval and acceptance of this thesis is contingent upon the candidate's submission of the final copies of the thesis to the Graduate College.

I hereby certify that I have read this thesis prepared under my direction and recommend that it be accepted as fulfilling the Master's requirement.

____ Date: ____________
[Committee Chair Name]
Master's Thesis Committee Chair
[Academic Department]

Acknowledgements

First, I'd like to thank Dr. Daewook Kim for giving me the opportunity to join the LOFT team and the South Pole Telescope Summertime Line Intensity Mapper project. Dr. Kim went above and beyond to find an amazing project that exposed me to real world lens design processes. Furthermore, I was able to share that experience and knowledge I gained in this very report. The world needs more educators like him.

Secondly, I'd like to thank my mother-in-law for all her support for my family. My wife and I both pursued graduate degrees while being full time employees and having our first child mid campaign. The task at the time seemed impossible, but my mother-in-law was always there to help care for our daughter on those days when studying, assignments, and exams came up. I am especially thankful for the nights she told us to take a load off while she happily watched our daughter.

Next, I'd like to thank my wife for her support and love throughout my graduate career and writing this report. Having someone going through the same experience as you always makes it easier. She pushed me when things got frustrating or tiring and always made sure I had an opportunity to work on what I needed, all the while supporting our family and her own grad career.

Finally, I'd like to thank my parents who left their war-torn country with 9 children for a better and safer life. I will never be able to repay such a sacrifice. The best I can do is take advantage of what you've given us, and ensure you live the most comfortable life possible.

Dedication

To my baby Leila Rae, you are the greatest source of light in my life.

Table of Contents

Abstract

The South Pole Telescope has played host to various cosmological surveys since 2007. Its primary goal is to detect the faint signals of the Cosmic Microwave Background. The interchangeable design of the SPT instrumentation made it easily adaptable to updates, as well as additions to the baseline design. The SPTpol design looked to upgrade the optical receiver to introduce sensitivity to polarization. The third generation, SPT-3G, made further enhancements by increasing throughput and adding new multi-chroic detector arrays in a larger focal plane area. Moving forward, the SPT was added to the Event Horizon Telescope network, and required a new set of optics and a new receiver. All of these surveys have helped to better shape our understanding of the universe, with the latter reaching the milestone of imaging the first black hole with unprecedented resolution. The future of the SPT now lies within the growing science of line intensity mapping. In this paper, I provide an overview of the optical system upgrades for each iteration of surveys, as well as initial design analysis of the future SPT-SLIM project.

1. Introduction

1.1 Overview of Off-Axis Cassegrain and Gregorian telescopes

The South Pole Telescope utilizes both the classical of-axis Cassegrain and Gregorian designs, therefore, it would appropriate to provide a high-level overview of both. The classical Cassegrain telescope design has a concave parabolic primary and a convex hyperbolic secondary, as shown in figure **1a**. Light is reflected off the primary towards the secondary, where the beam is reflected towards the secondary mirror axis. The light is focused here and is known as the Cassegrain focus. An advantage of the Cassegrain design for observatories is that removing the secondary mirror gives access to prime focus. The prime focus is essentially the focus of the primary mirror being used, and it provides a larger field of view. The classic Gregorian reflecting telescope design is demonstrated in figure 1b. Light enters the system, where it is gathered and reflected at the primary parabolic mirror. A secondary ellipsoidal mirror is placed outside of the focal point of the primary and reflects the light towards the image plane located on the secondary mirror axis.

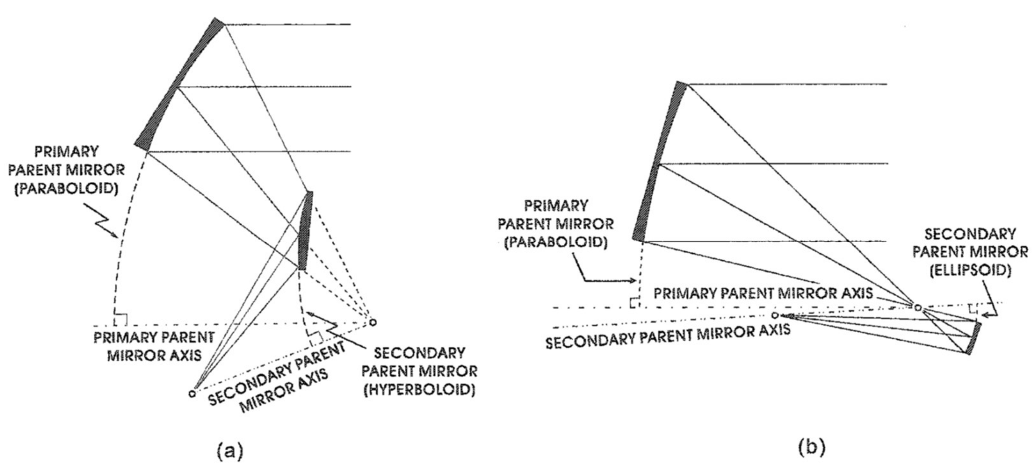

Figure 1. Two classical off-axis configurations. (a) Off-axis Cassegrain (b) Off-axis Gregorian

The parabolic shape of the primary mitigates spherical aberrations. The dominant aberration for off-axis reflecting telescopes is linear astigmatism. [1] This comes from the tilt of the tangential and sagittal images surfaces inherent from the tilted design. Though third order coma and astigmatism are also present, this second order astigmatism degrades performance more substantially. [2] Fortunately, a design that satisfies the following equation eliminates the tilt angle of the astigmatic image planes.

$$\frac{l_1}{R_1} * \sin 2i_1 = \frac{l_2}{R_2} * \sin 2i_2 \tag{1}$$

where l_1 and l_2 are the distances of the common focus from the primary and secondary mirrors, i_1 and i_2 are incident angles for the primary and secondary mirrors, and $R_1$and R_2 are the radius of curvature of the primary and secondary mirrors. [2] Once this second order aberration is gone, the system then behaves similarly to the on-axis case and can be optimized as such, as shown in figure 2. [2]

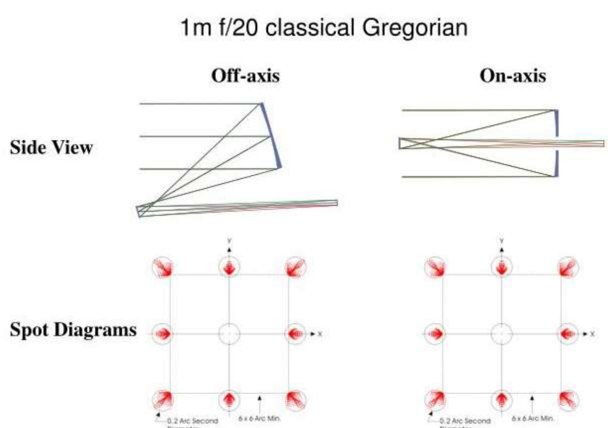

Figure 2. Comparison of Spot Diagrams. The off-axis case is equivalent to the on-axis in terms of aberrations when linear astigmatism is eliminated.

1.2 Baseline Objective: The SPT-SZ

The process of recombination, when the universe allowed the first stable atoms to form 380,000 years after the Big Bang event, led to a massive production of light as electrons joined nuclei. [3] We see this light many years later as the cosmic microwave background. This noise comes from all directions and is nearly isotropic since recombination occurred everywhere. There are, however, anisotropies that can provide information on how much dark energy, dark matter, and ordinary matter are contained in the universe. [3] The SPT's initial objective was to conduct a survey of galaxy clusters through their Sunyaev-Zel'dovich (SZ) signatures. The SZ effect occurs when a galaxy cluster interacts with photons of the CMB. They scatter off of the free electrons present in the galaxy's hot gasses. [4] This leads to a signature along the line of sight of a galaxy cluster where the CMB appears dim at low frequencies and brighter at high frequencies. [4]

1.3 SPT-SZ Design

The South Pole Telescope (SPT) is a 10 m diameter, wide-field, offset Gregorian telescope located at the Amundsen-Scott South Pole station in Antarctica. [5] It is optimized for observations in the microwave and submillimeter wave and is purposed to detect the faint signals emitted by the Cosmic Wave Background. The South Pole is unique in that its location provides an ideal site for these observations. This is due to its altitude, sitting at 2835 m, and low precipitable water vapor. [5] Additionally, the lack of a 24-hour day-night cycle requires an almost negligible need for sun-avoidance measures and produces low noise atmospheric conditions. [5] Light from the primary is directed through a window that has > 99% transmission average in the 90, 150, and 220 GHz frequencies. Past this, cooled IR shaders and blockers are used to redirect reflected light away from the focal plane. The light arrives at the 1 m secondary, which is cooled and acts as the stop. From here, light propagates towards the receiver cryostat. Since the focal plane of a Gregorian telescope suffers from field curvature, a high-density polyethylene (HDPE) window that has an anti-reflection (AR) coating with a performance of < 1% reflection average across all three frequencies, is placed before the cryostat. [6,7] This lens reimages the light at the Gregorian focus to make a telecentric focal plane. This better couples into the feedhorns of the detector array. It also reduces the final focal length, allowing us to use a slightly higher secondary magnification, which increases the clearance between the receiver and the beam. [5] Performance from this configuration yields a roughly 1 deg^2 diffraction limited field of view at 150 GHz, or 2 mm. Figure 3 shows the system as well as its performance using the spot diagram as a metric.

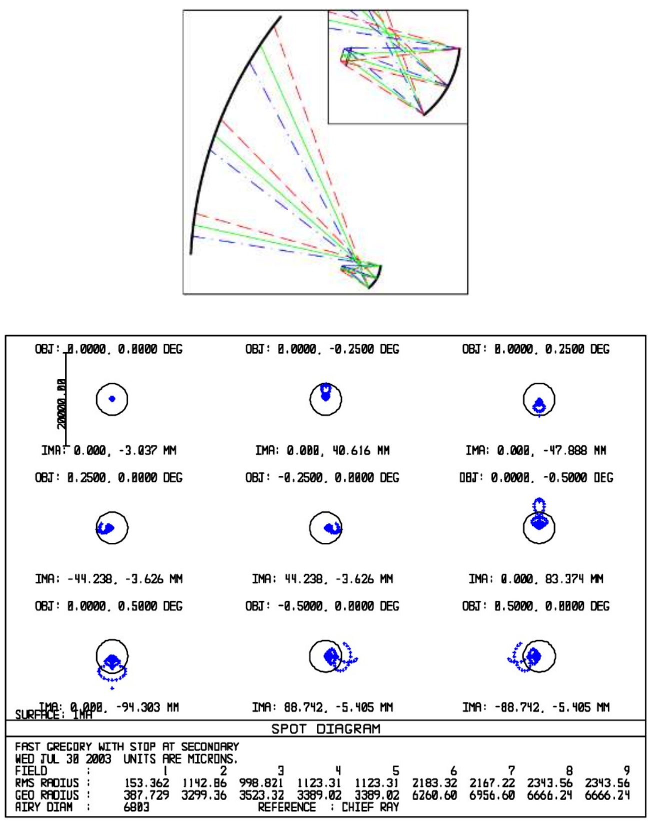

Figure 3. SPT Baseline. (Top) YZ view of the optical model (Bottom) Spot Diagram as a function of field position.

The detector consists of 960 spiderweb bolometers with Transition-Edge Sensors (TES). [6] A bolometer detects electromagnetic radiation by an absorption of radiation that increases its temperature. The temperature increase is related to the energy absorbed per unit mass via the specific heat capacity. [8] TES was utilized due to its simple fabrication, cheap cost, well controlled responsivity, and insensitivity to vibration. [6] The detector is broken up into six wedges, with each wedge having 160 bolometers shown in Figure 4. The configuration of the wedges held so that one wedge operated at 90 GHz, one at 220 GHz, and four at 150 GHz. Atop each wedge, is a horn array to assist further in coupling radiation into the detectors. [7]

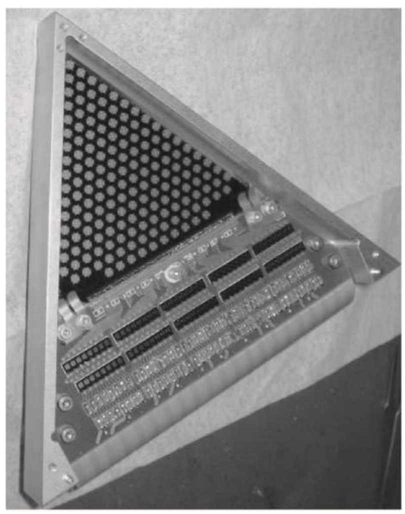

Figure 4. Detector wedge for the SPT-SZ

2. Evolution of Objectives and Instrumentation

2.1 SPTpol

2.1.1 Objective

The SPTpol instrumentation was installed in January of 2012, and consisted of a new a two-color, polarization-sensitive bolometer receiver. The new polarization capabilities allowed for the decomposition of measurements into “E-mode” and “B-mode” signals, which contain a wealth of information about the initial conditions, content, and evolution of the Universe. [9] Furthermore, this led to constraints of various fundamental cosmological parameters such as the mass and number of neutrinos, the primordial power spectrum, and the density and equation of state of dark energy. [9]

2.1.2 SPTpol Design

The optical design did not change much from the previous SPT-SZ, with the most notable upgrade coming with the detector. A 1.5 m guard ring was installed around the 10 m primary, as well as intentionally underfilling to 8 m, in attempt to further ground shield. [7] The new camera, pictured in Figure 5, holds 768 feedhorn-coupled, dual-polarization pixels, each consisting of two transition-edge sensor (TES) bolometers. The outer ring of the detector holds 180, 90 GHz pixels mounted on top with a contour circular feedhorn. [9] The inner ring is comprised of 588, 150 GHz pixels with mounted corrugated feedhorns. [9] The dual polarization of each pixel allows the camera to be sensitive enough to measure the polarization anisotropy of the CMB on angular scales from an arcminute to several degrees, while continuing to take sensitive measurements of temperature anisotropy. [7]

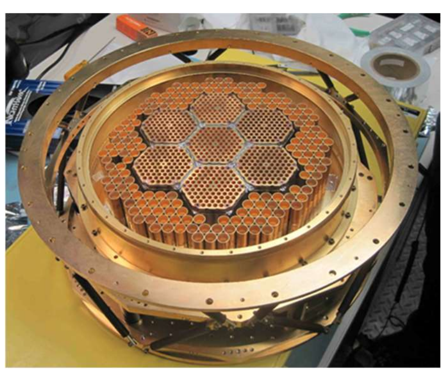

Figure 5. New SPTpol detector with 150 GHz and 95 GHz pixels

2.2 SPT-3G

2.2.1 Objective

The SPT-3G is the third-generation survey receiver on the SPT following SPTpol. The SPT-3G sought to provide even higher resolution observations of the CMB. Precise measurements of the different anisotropies in the CMB provide constraints on the Lambda-Cold Dark Matter (ΛCDM) model. [3] It also provides a test of consistency for the ΛCDM. The SPT-3G optical design provides arcminute resolution to help detect these measurements while also having the ability to detect galaxy clusters, millimeter-wave bright galaxies, and a variety of transient phenomena. [10]

2.2.2 SPT-3G Optical Design

The SPT-3G optical design kept the off-axis Gregorian approach with a few updates. The optical model is shown in Figure 6. Once again, the light is reflected off the 10 m primary mirror, onto a new 2 m, ambient temperature, ellipsoidal secondary.[10] The secondary then reflects to a 0.8 m cooled tertiary flat mirror, which reflects the light once more towards the optic cryostat. [10] Within the cryostat are IR blocking filters, alumina lenses, a 4K cold Lyot stop, and, finally, the detector array. [11] A Lyot stop is used to reduce the amount of flare caused by diffraction of other stops and baffles. [12] The light enters the 30 mm thick (HDPE) window, where the Gregorian focus is reimaged, filtered, collimated, and sent down to the new, multi-chroic detector. [10] The new optics increases throughput by a factor of 2, with an additional increase of 2.8 deg^2 field of view. [10]

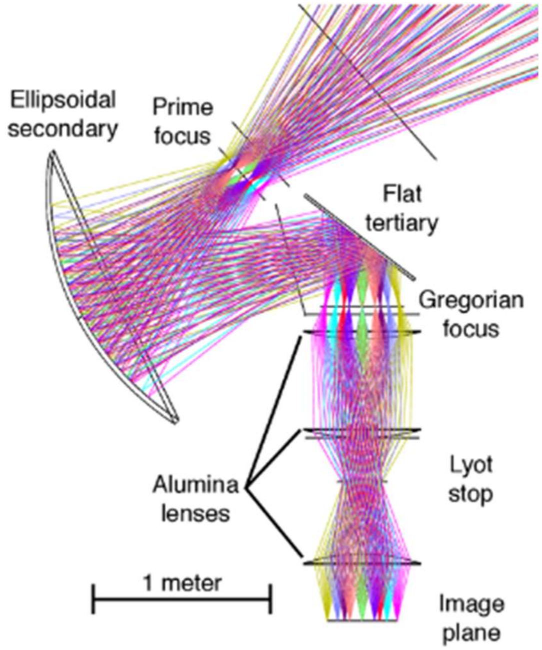

Figure 6. SPT-3G optical model.

The increase in field of view (FOV) produces a much larger 30 mm focal plane, therefore, another upgrade to the systems camera was implemented. The new multi-chroic detector is optimized at 150 GHz, but also operates at 95 and 220 GHz with good performance and is shown in Figure 7. The detector is made of 10 wafers each with 269 pixels. [10] This is an increase from the SPTpol's 768 to a new total of 2690 pixels. [10] Each pixel is made of six detectors that measure polarization at 95, 150 and 220 GHz. The camera now had a total of 15,234 total bolometers, which made it extremely sensitive to electromagnetic radiation. [13] The design showed excellent performance for its objectives, as shown in Figure 8. [11]

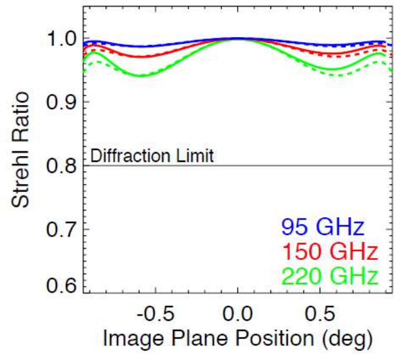

Figure 7. SPT-3G performance. Strehl ratios for the bands at 95 GHz, 150 GHz, and 220 GHz are 0.98. 0.96, and 0.93 respectively.

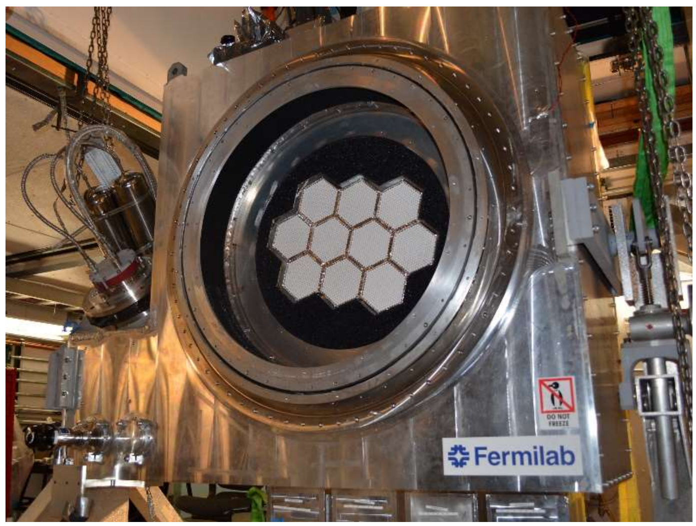

Figure 8. SPT-3G detector array

2.3 SPT VLBI Receiver

2.3.1 Objective

The Event Horizon Telescope (EHT) is a very-long-baseline interferometry (VLBI) experiment that aims to observe supermassive black holes with an angular resolution that is comparable to the event horizon scale (EHS). [14] The angular resolution of a telescope is inversely proportional to its diameter, so to image objects at the EHS, you would theoretically need a radio telescope the size of earth or greater. Instead, the extremely weak signals from a distant radio object are received at the individual telescopes of an interferometer system, amplified, translated in frequency to a low frequency band, and then sent to a special purpose correlator, as shown in Figure 9. [15] Pairs of this information are combined between telescopes to produce interference patterns. Telescopes close together produce wide fringes, while those that are far apart produce more narrow fringes. The pair of telescopes within the network are all at different distances and orientations, and thus create several different patterns. These patterns are combined, and Fourier transformed by a high-speed computer to create an image.

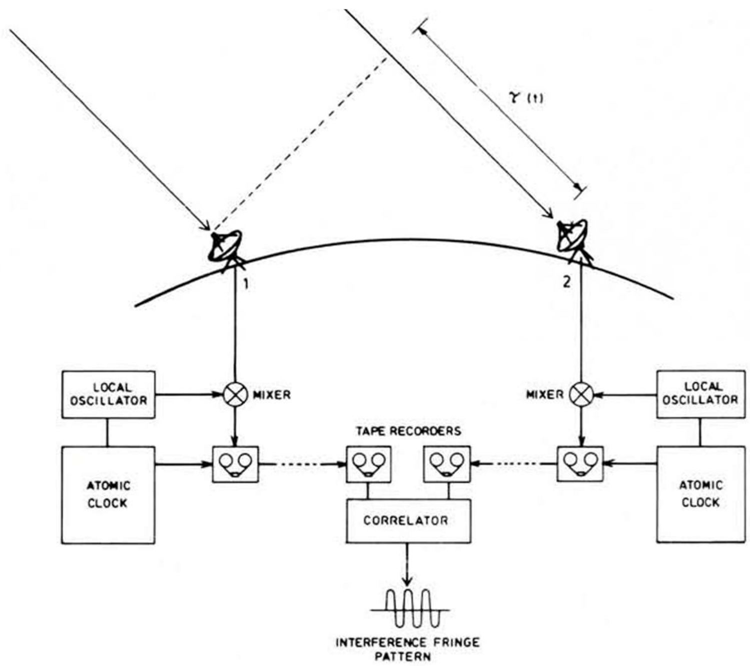

Figure 9. A diagram of VLBI operations

Since the South Pole has low precipitable water vapor and a stable atmosphere, EHT decided to include the SPT in its VLBI network. [16] Unfortunately, the SPT-3G's baseline design was not fit to jump right into EHT interferometric operations. Mainly, the transition-edge sensor (TES) array was insensitive to incoming radiation phase, a characteristic needed to perform interferometric measurements with other telescopes in the chain. [16] Thus, the need to upgrade the receiver arose. The upgrades that followed included a new secondary mirror, a new tertiary mirror, and a new receiver assembly.

2.3.2 VLBI Configuration Optical Design

The SPT was designed only to illuminate its proper CMB camera. To guide the collected light from the primary to a new, updated receiver, a bent Cassegrain design was utilized around the current optics. A new hyperbolic secondary and ellipsoidal tertiary were installed inside the SPT cabin to modify the beam path. The new secondary blocks the previous SPT-3G secondary mirror and reflects the beam from the primary to the new tertiary mirror. The beam is then directed towards the feed horns of the new VLBI receiver. [6] Figure 10 illustrates the locations of the hardware to create the new beam path. [16] The receiver operates at both 230 and 345 GHz frequency bands that helps facilitate dual-polarization, two-single-sideband observations. [16] The tertiary mirror is mounted to the top of the receiver housing and can rotate the mirror around the optical axis so that it focuses the beam towards either 230 or 345 GHz side of the receiver.

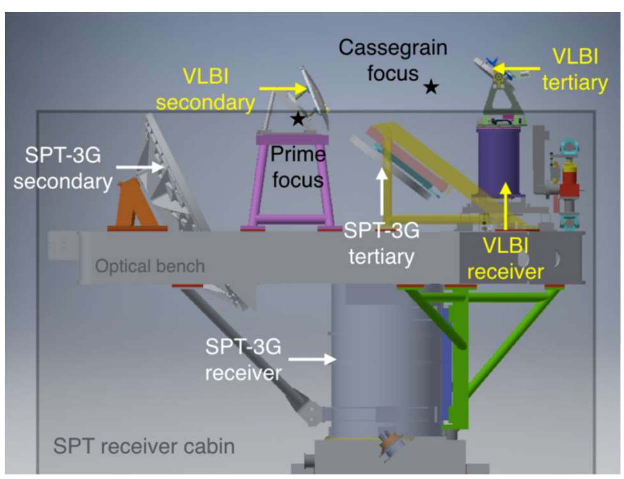

Figure 10. New optics setup for the SPT VLBI detector.

Since the VBLI optical configuration was defined for on-axis use, it boasts a Strehl ratio of 0.98 when there is no deviation from the central angle. As we travel off the central angle, field dependent aberrations degrade the wavefront very quickly, as shown in Figure 11. [9] One arcminute off-axis drops the Strehl ratio to 0.81, while two arcminutes down results in degradation of the Strehl ratio to 0.44. [17]

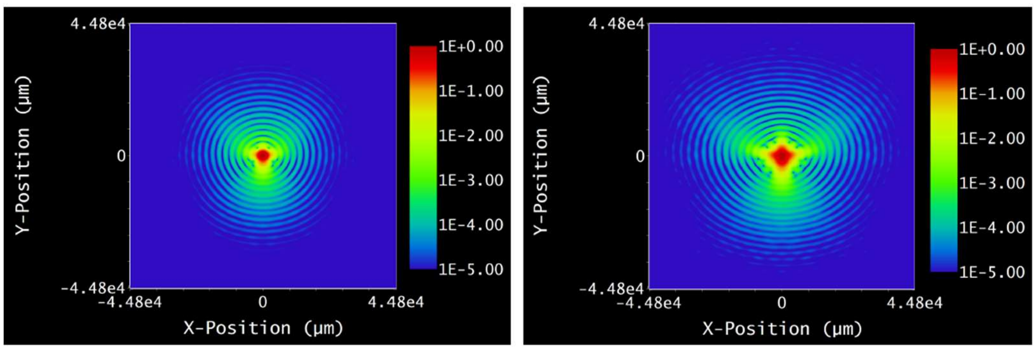

Figure 11. Performance of the VLBI detector (Left) Strehl Ratio at 1 arcminute (Right) Strehl Ratio at 2 arcminutes.

2.4 SPT-Summertime Line Intensity Mapper

2.4.1 Overview of Line Intensity Mapping

LIM is a relatively new technique that can expected to provide mapping of large-scale structures (LSS), which can be used to further constrain multiple parameters in the ΛCDM model of cosmology. [18] Traditional survey methods usually involve imaging bright objects directly. LIM provides measurements of the spectra of light coming from an area of the universe to map what elements are present, as well as red-shifting to determine distance.

A line intensity map traces the cumulative emission of a given emission line from all galaxies in a target region. The target galaxies trace the matter over-density, allowing for an inference of the large-scale structure of dark matter. To obtain redshift information, we can compare the observation frequency υ_{obs} to the rest-frame frequency υ_{rest} of the target line, through the following relation [18]:

$$z = \frac{\upsilon re}{\upsilon obs} - 1 \tag{2}$$

There are many advantages to using the LIM technique. One is that it is sensitive to all sources of emission in the line, therefore, it can pick up on faint signals. [19] It also does not require a high angular resolution. Instead, it uses all incoming photons from any source within the field of view, obtaining tomographic line-of-sight information from targeting a known spectral line at different frequencies. [19, 20] Lastly, typical galaxy surveys observe in the IR, whereas LIM observes microwaves. This has the potential to uncover new scientific truths as the technique matures over time.

2.4.2 Objective

SPT-SLIM is a pathfinder instrument to demonstrate the use of 36 on-chip spectrometers observing from 110 – 190 GHz with R=300 spectral resolution for mm-wave line intensity mapping (LIM). [17] Currently in its design phase, it is planned to target carbon monoxide (CO) rotational transitions from high-redshift galaxies. These originate in dense molecular clouds and trace the sites of star formation. SPT-SLIM is expected to detect rotational transitions from $0.3 < z < 0.9$, $0.9 < z < 1.8$, and $1.6 < z < 2.8$, shown in Figure 12. [21] These measurements have the potential to inform models of the CO luminosity function and the cold molecular gas fraction as a function of redshift for the full population of galaxies. [21]

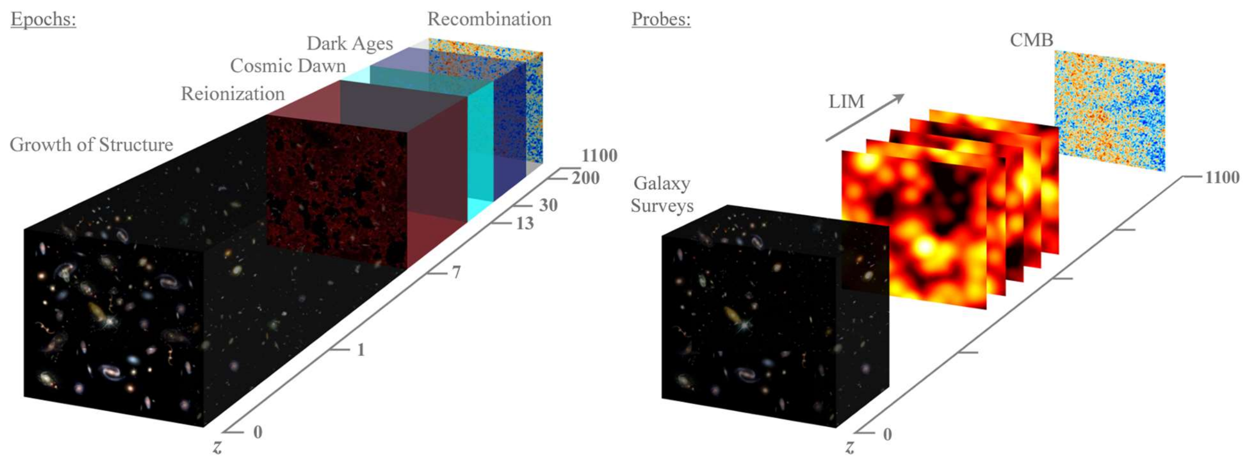

Figure 12. (Left) Epochs of the universe. (Right) Redshift range z>3 is generally unexplored and will be surveyed by SPT SLIM.

2.4.3 Optical Design

The SPT-SLIM is still in the design phase at the time of writing. This design phase can be split into two phases that will be analyzed in detail later in the report. Phase 1 consists of the original design developed at the beginning of the SPT-SLIM effort. Phase 2 sees an update to the design that simplifies and simultaneously enhances the performance of the system. This section will seek to provide the configuration of the designs and analyses respective to them.

2.4.3.1 Analysis of Two Mirror Telescope with Free Form Optics

A free form optic is defined as any non-rotationally symmetric surface. [22] Analysis of two different configurations utilizing free form optics and one configuration utilizing rotationally symmetric traditional optics was done. Figure 13 shows each free form configuration.

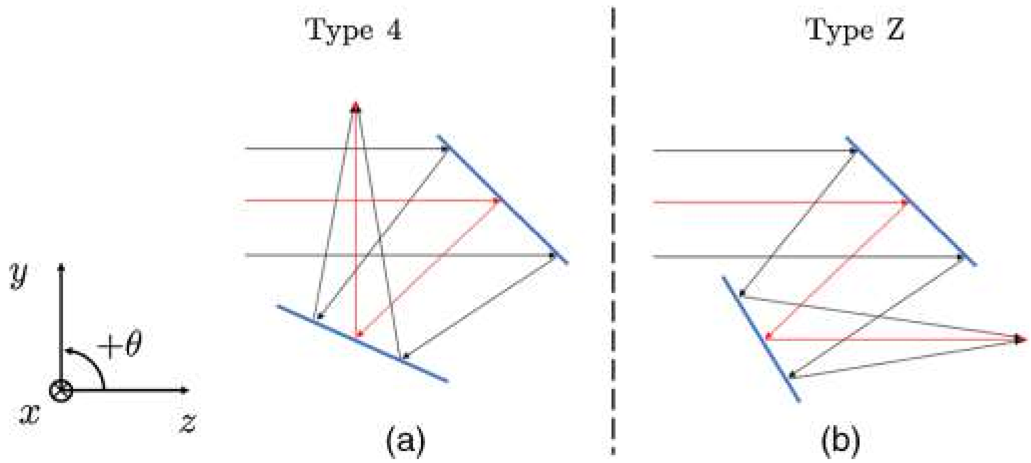

Figure 13. (a) The Type 4 telescope configuration (b) The Type Z telescope configuration

For each design, the FFOV was plotted as a function of F/# as well as system volume as a function of F/#. The free form designs were also optimized with and without the constraint of tele-centricity. Results showed that the Type Z and Type 4 held a higher FFOV at lower F/#'s than the traditional optical design, as well as providing a smaller form factor. FFOV for the free form designs are roughly level at the faster F/#'s. [23] The advantage, therefore, comes in comparison with system volume. The Type 4 is substantially more compact than the Type Z for telecentric designs. [23] Figure 14 shows the results of the study.

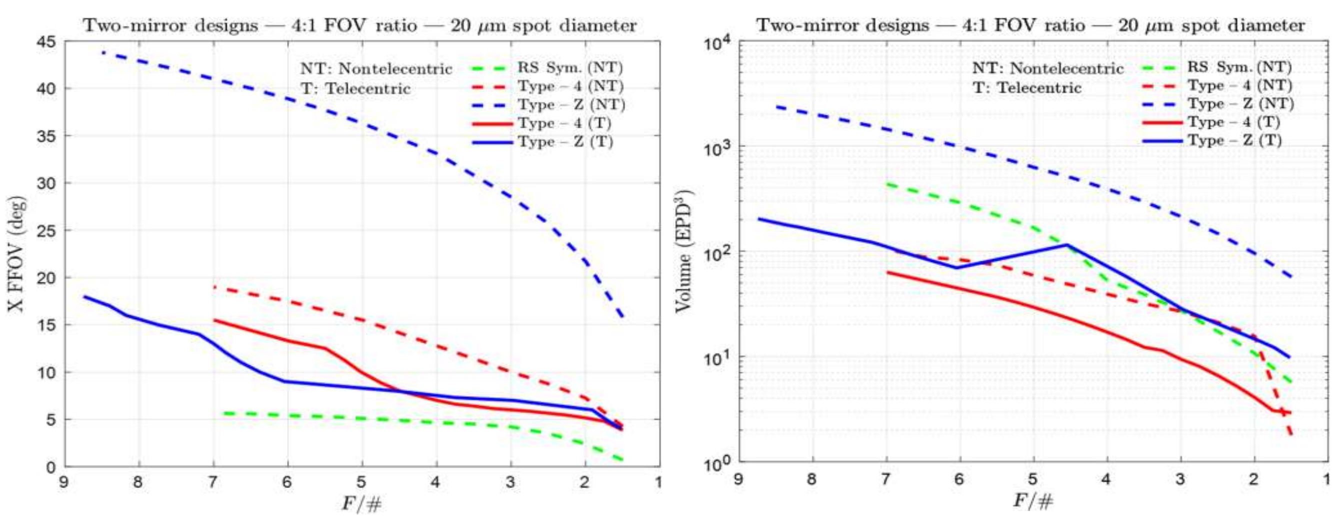

Figure 14. Performance vs F/#. (Left) FFOV as a function of F/# for all three types of telescopes. (Right) System Volume as a function of F/# for all three types of telescopes.

2.4.3.2 Phase 1: The Figure Four Configuration

The new SPT-SLIM designed needed to correct the field-dependent aberrations that the VLBI design was culpable of. Based on the analysis of the previous section, the design team at the Wyant College of Optical Sciences at The University of Arizona proposed a solution to add a free form corrector and a fold mirror after the Cassegrain focus, essentially producing the figure four design scheme shown in Figure 15. [17] This would reduce the angle of incident rays impeding on each optical surface [17]. Analysis of deformations in surface sag against a 36-term Zernike polynomial best-fit sphere showed to be ±25 μm . The bent design of the figure four inherently produces field coma and astigmatism by the primary and secondary mirrors. The freeform corrector substantially limited these aberrations. [17]

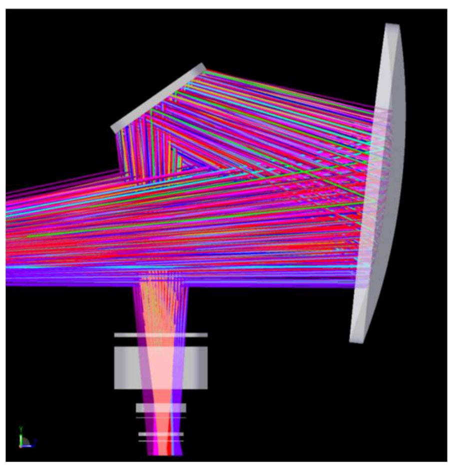

Figure 15. Initial Figure Four design for the new SPLT SLIM.

Aside from correction of aberrations, the new experiment and instrumentation sought out by SPT-SLIM required a considerably larger throughput, or faster system, than the VLBI configuration produced. To accomplish this, mirror 3 (hereby known as M3) and mirror 4 (hereby known as M4) were varied in both position and orientation relative to the Cassegrain focal plane. Using merit functions for global coordinates, angle of incidence, and aberrations the design was optimized through damped least-squares (DLS) optimization in Ansys Zemax. The result was the system F/# being sped up from F/4 to F/2, and diffraction limited across a ±24 arcminute full FOV, evident in Figure 16. These improvements to performance were deemed enough for the obligations of SPT-SLIM [17]. We know with optimization, however, that there are always trade-offs. The final design did have residual field curvature and tilt at the edge of the field, but fortunately it was decided to a negligible degree. With the aberrations of the system reduced and the throughput increased, the next figure of merit the team wanted to analyze was the spillover energy at each mirror, quantified as a percentage of energy lost from one surface to the next [17].

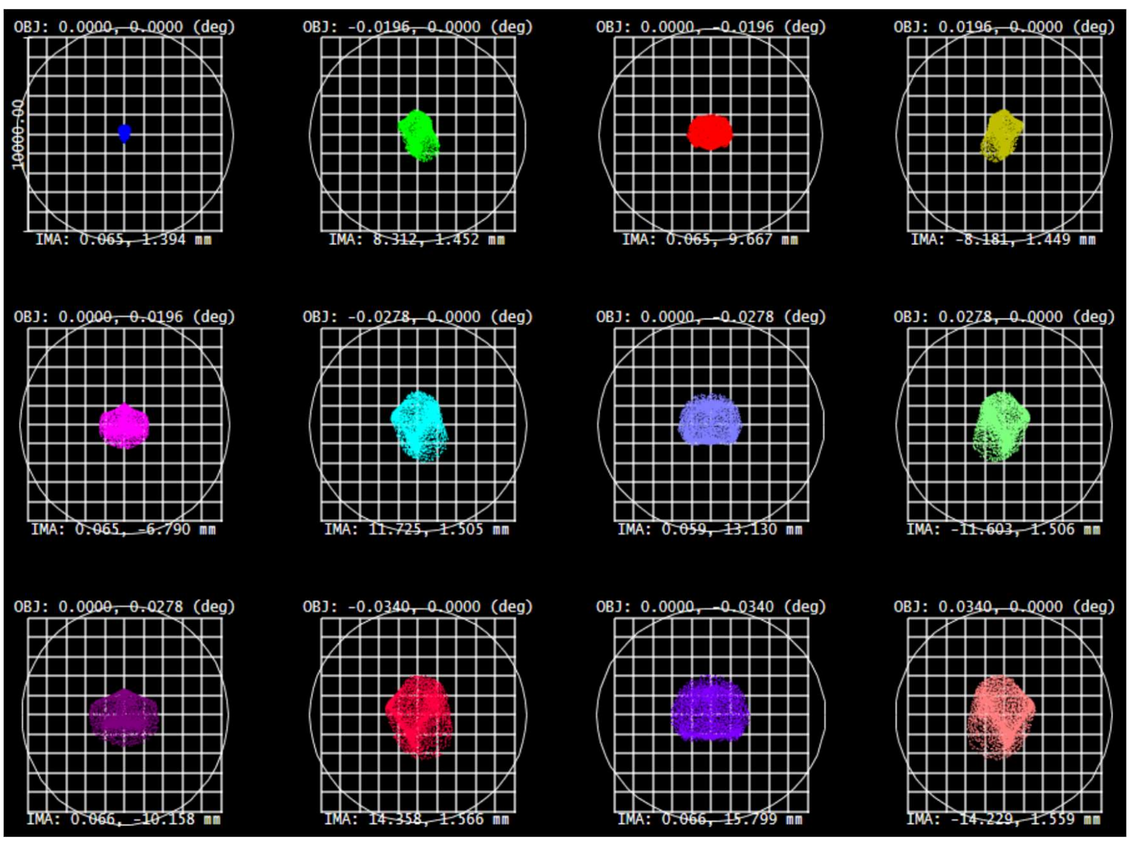

Figure 16. SPT SLIM figure four RMS spot size across the FOV and waveband of 1.6 – 2.7 mm

The SPT-SLIM detector is a hexagonal close-packed array, where each of the 18 spatial pixels is sensitive to both polarizations (36 spectrometers total) [21]. Gold plated conical feedhorns guide radiation to the spectrometers. The design covers the 120–180 GHz band with high efficiency. The new detector consists of three submodules, containing 6 dual-polarization pixels, coupled to 12 spectrometers. The length of each filter-bank is 80 mm, oriented radially from the focal plane center, as seen in Figure 17.

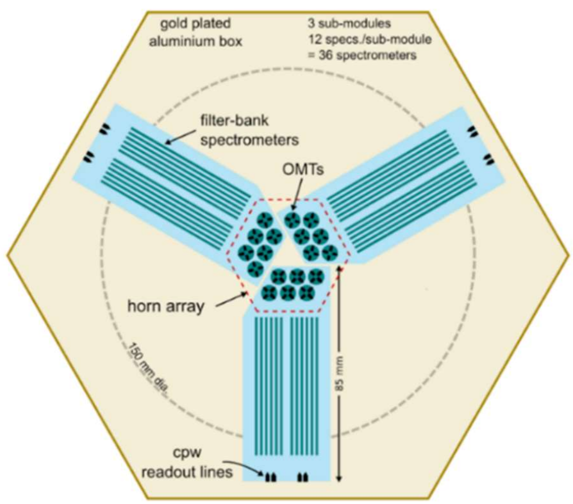

Figure 17. Model of the new SPT SLIM detector

2.4.3.2.1 Spillover Analysis of Figure-Four Configuration

This type of analysis would have to be done on a time reversed model of the system. This is because the system will be dealing with relatively longer wavelengths. Since wavelengths typically interact more with obstacles closer to their size, these longer wavelengths will suffer from significant diffraction effects. Thus, the team looked to Ansys Zemax's Physical Optics Propagation (POP). POP analysis is a powerful Sequential Mode tool for analyzing beam propagation and fiber coupling. It uses diffraction calculations to propagate a wavefront through an optical system surface by surface [24]. The parameters for POP analysis were first order approximation of an individual pixel in the feedhorn. With an F/2 at 150 GHz, or 2 mm wavelength, the beam waist was calculated as 6.2 mm in diameter, located 460µm inside the feedhorn [17]. A 1 W beam was launched for each test case. The analysis incorporated an optimized focal plane layout to maximize sensitivity. 12 pixels, each containing an on-chip spectrometer, are assembled at the feedhorn array of the SPT-SLIM instrument, shown in Figure 18. [17, 25]

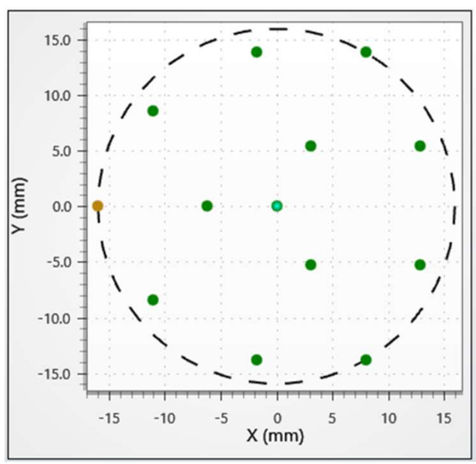

Figure 18. (Left) Assembly of the 12 pixels across the feedhorn array

The procedure consisted of launching a beam first from the center pixel, followed by the leftmost pixel of the field, concluding with the symmetric rightmost pixel of the field. The team's goal was to keep spillover at M3, M2, and M1 at less than 1%. To help with this, it was decided the spillover at M4 could be intentionally large [17]. This was due to the fact that the cold Antarctic sky radiates at levels way below other background sources. Each case's respective spillovers percentages are shown in Figure 19. The second and third cases, as expected, suffer from greater spillover than the on-axis case. Furthermore, the rightmost pixel case suffers from the greatest spillover at M4. Nevertheless, the spillover requirement is met in each instance [17].

By this point in the design, the throughput of the system was at F/3.5 [17]. While meeting everything met design requirements, there was still plenty of design margin to work with. The team sought out to increase the size of M4, therefore, leading to a decrease in spillover. Consequently, this led to speeding up throughput. M4 was increased by 40% in diameter, which dropped the spillover by roughly 13% and stepped the F/# down to F/2.5. Once again, a trade off was required. The increase in reflector size induces an increase in beam size. This leads to an increase in aberration effects. Fortunately, those increases were considered acceptable.

Surface	Power (W)	Power Spillover (%)
Launch	1.000	0.000
M4	0.648	35.20
M3	0.644	0.361
M2	0.642	0.253
M1	0.640	0.205

Surface	Power (W)	Power Spillover (%)
Launch	1.000	0.000
M4	0.532	46.70
M3	0.528	0.405
M2	0.526	0.229
M1	0.524	0.018

Surface	Power (W)	Power Spillover (%)
Launch	1.000	0.000
M4	0.572	47.10
M3	0.567	0.454
M2	0.565	0.226
M1	0.560	0.504

Figure 19. Spillover analysis. (Top) Spillover from the center virtual pixel (Middle) Spillover from a pixel at the leftmost extent of field (Bottom) Spillover from a pixel at the rightmost extent of field

The figure-four approach was selected due to a desire to not make any changes to M1 and M2. To meet a proper throughput for LIM experiments, M3 was developed as a curved optic. The

M4 flat mirror was used in combination to reduce astigmatism from the angle required of M3 and to fold the beam path. While requirements were met in the analyses of this design, the coordinates of the model were difficult to maintain properly. A proper coordinate system is required for an accurate POP analysis in a time reversed model. It was then recommended to revisit the configuration of M2. Interest in exploring an M2 redesign by changing its curvature grew. This would ultimately lead to the next, and current design effort for the SPT-SLIM.

2.4.3.3 Phase 2: The 3-Mirror Configuration

The redesign of the SPT-SLIM model aimed for a simplified model and is shown in Figure 20**.** The curved M3 optic was dropped and the curvature of M2 was changed, making it the freeform corrector. M3 changed into a flat mirror to fold the beam path into the cryostat receiver. M4 was eliminated altogether. Through another set of iterations, the M2 curvature was optimized, and the final speed of the system was F/2.85. The team at the University of Arizona were kind enough to allow me to join and assist in analysis of the SPT-SLIM redesign. The rest of this section details those analyses.

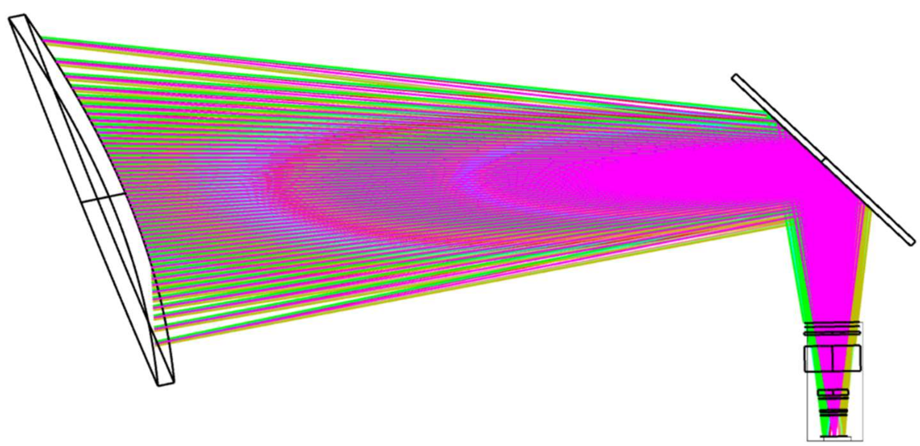

Figure 20. The second iteration of the SPT SLIM design.

2.4.3.3.1 Overview of Tolerance Analysis

Optical tolerancing determines optical performance degradation due to external environments [27]. It ensures that appropriate optical performance will be achieved considering all the manufacturing errors involved in the system. It helps determine tolerance ranges for fabrication and alignment. Typically, the process involves establishing a figure of merit, calculating sensitivities, and estimating performances. The parameters are x and y-decenter, and α, β, and γ-tilt, despace and focus [26]. A general coordinate system for these parameters is displayed in Figure 21. Component sensitivities are explored by individually implementing tolerance parameters for each mirror. Afterwards, Monte Carlo simulations are run to analyze system performance when all the tolerancing simultaneously affects the system [26].

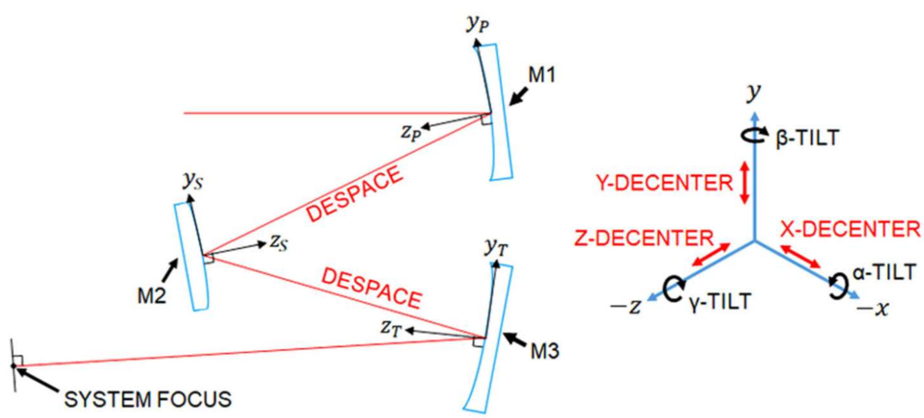

Figure 21. General coordinate system for decenter, despace and focus for tolerance analysis.

2.4.3.3.2 Individual Component Tolerancing of 3-Mirror Configuration

The parameters for our analysis did not include despace or focus, and the figure of merit used was the RMS spot radius. The analysis starts with decenter introduced in M2, M3, and the cryostat window. When a perturbation is being introduced in a particular component, all others are left untouched. The process is then repeated for tilt. Each perturbation is relative to the primary mirror, known as M1 in this configuration. For each process, no compensation methods were used in the analysis. This makes for a more conservative approach because we do not utilize any degrees of freedom to enhance the spot size measurement.

The data was plotted using a polynomial fit, with coefficients generated by the function in Zemax. [27] This function determines tolerance sensitivity at 6 points, spanning our perturbation range of -1 mm to 1 mm. The 5-Term polynomial utilized is of the form following:

$$P = \mathrm{A} + \mathrm{B}\,\Delta + \mathrm{C}\,\Delta^2 + \mathrm{D}\,\Delta^3 + \mathrm{E}\,\Delta^4 \tag{3}$$

where Δ is the tolerance perturbation value and P is the resulting criterion. [26] This method helps to observe trends in data easier. In these analyses, it should be noted that the nominal spot size is valued at 0.8884 mm. Figure 22 shows sensitivity analysis for M2. Given that this component is the largest in size relative to the other two, it was expected for the system to be sensitive to perturbations to this component. For decenter, negligible change to RMS spot size is seen across the x-axis. The largest differences come in the z-axis and y-axis, where spot size fluctuates up to 1 mm and 0.5 mm respectively. The tilt follows a parabolic trend as expected, with spot sizes reaching roughly 2.5 mm increase from the nominal. Next, our analysis of M3 is displayed in Figure 23. RMS spot size varied in the z-axis at ±0.04 mm off nominal. Tilt varied less, with the greatest off nominal value at roughly 0.1 mm. Lastly, we analyzed the HDPE cryostat window, shown in Figure 24. Being the smallest of the components, it was not expected for the system to be substantially sensitive to perturbations. Decenter spot sizes varied at most 0.06 mm, while the tilt had negligible spot size differences. Data trends show that the spot size in the z-axis was completely independent of tilt.

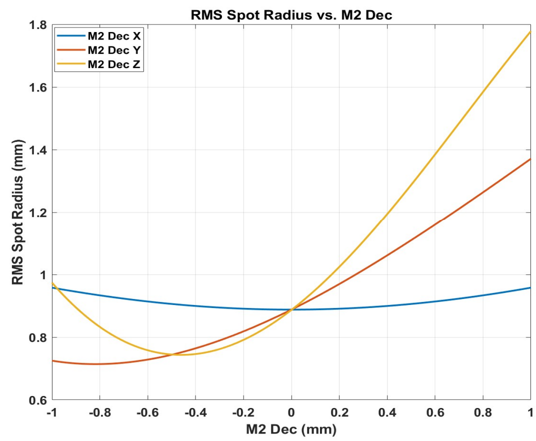

Figure 22. Tolerance analysis results for freeform corrector M2

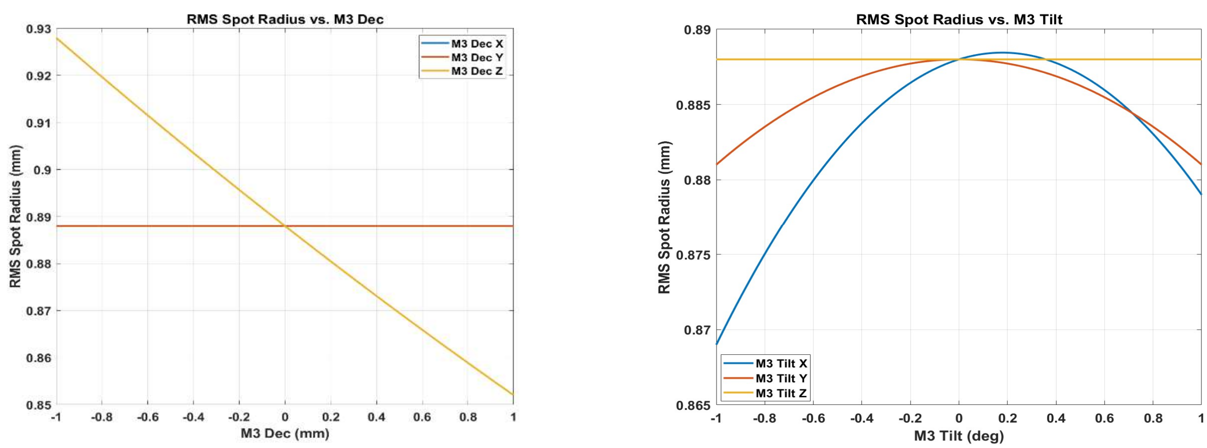

Figure 23. Tolerance analysis results for flat mirror M3

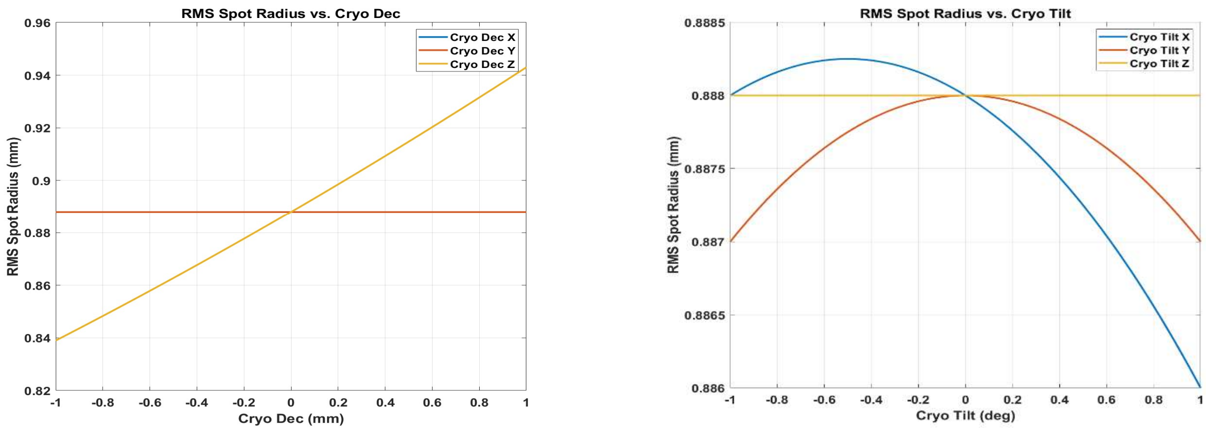

Figure 24. Tolerance analysis results for HDPE lens

It was desired to maintain a spot size within roughly 10% of the optimum 0.8884 mm. Per the results, this meant a position accuracy requirement of ±0.3 mm for M2, and greater than 1 mm for M3 and the cryostat. The tilt requirements would be ±0.2 degrees for M2, and greater than 1 degree for M3 and the cryostat.

Position and tilt for M2 is controlled by optical bench linear actuators. These actuators stop moving to the commanded position once it is within 0.02 mm of the target, while the angular tilt resolution is 0.0011 degrees. Both are well within the requirements for M2. M3 is proposed to be rigidly mounted to the cryostat top flange, with its position and tilt to be controlled by screws and shims. The screws have a resolution of 0.2 mm. The design time was also confident that the tilt could be controlled by shimming and could achieve a resolution of 0.04 degrees. Once again, these meet the requirements of the analysis. Finally, the cryostat, or detector package, does not have a horizontal degree of freedom. This is not an issue, as the data suggests that the spot size is insensitive to displacement in the x-axis. Vertical displacement is controlled by shims that can be easily converted to have a resolution of 0.2 mm. Tilt is controlled by 3 shimming points, whose angular resolution is 0.08 degrees. Both are in specification of the requirements levied.

2.4.3.3.3 Spillover Analysis of 3-Mirror Configuration

Like the figure four configuration, a spillover analysis using POP was conducted on the new design. In this analysis, the team was concerned with the edge cases of the bandwidth of the detector. This corresponded to 110 GHz and 190 GHz, or 2725 µm and 1578 µm respectively. At 110 GHz, the team at Fermilab calculated the beam waist to be 3.14 mm located at 2.73 mm inside the feedhorn. At 190 GHz, the beam waist radius was 2.98 mm and was located 7.35 mm inside the feedhorn. For both cases, POP was conducted on-axis, and off-axis at the edge of the field. A 1 W beam was launched from the pixel location on the feedhorn, propagated to M3, then M2, and finally ending at M1. Tables 1 and 2 show the amount of spillover at each reflector as a percentage of energy lost after propagating to each surface. At 110 GHz, there is a loss of nearly a quarter of power loss at M2 and a considerable loss at M3 for both on and off axis cases.

On-axis @ 190 Ghz			On-axis @ 110 Ghz		
Surface	Total Power (W)	% Spillover	Surface	Total Power (W)	% Spillover
Beam Launch	1	0	Beam Launch	1	0
M3	0.99443	0.557	M3	0.83116	16.884
M2	0.93709	5.76612	M2	0.60905	26.7229
M1	0.92043	1.77784	M1	0.55332	9.15032

Table 1. Percentage of spillover at each surface on-axis for both 110 and 190 GHz frequencies

Off-axis @ 190 Ghz			Off-axis @ 110 Ghz		
Surface	Total Power (W)	% Spillover	Surface	Total Power (W)	% Spillover
Beam Launch	1	0	Beam Launch	1	0
M3	0.95964	4.036	M3	0.78264	21.736
M2	0.91453	4.70072	M2	0.58403	25.3769
M1	0.9209	0.696533	M1	0.54528	6.63493

Table 2. Percentage of spillover at each surface off-axis for both 110 and 190 GHz frequencies

2.4.3.3.4 Optimizing the Aperture Size and Shape of M3

It was desired to maintain spillover at M1 and M2 to less than 2% at the upper and lower bands of the detector. There was no requirement levied on M3 spillover. The increase in spillover was attributed to the increase in the size of M3 from the previous configuration. Though the efficiency was increased, it was at the cost of spillover at M1 and M2. A new analysis was done to model the effects of decreasing the M3 diameter and its effect on M1 and M2 spillover. Suggested dimensions were 160 mm, 180 mm, 200 mm, and 260 mm. The idea was to see if making M3 similar in size to M4 in the previous configuration would improve spillover.

The spillover comparison as a function of optic size for the figure four and 3-mirror configurations are shown in Figure **25**. The new configuration gives similar performance as the figure four for an optic 180 to 200 mm in size.

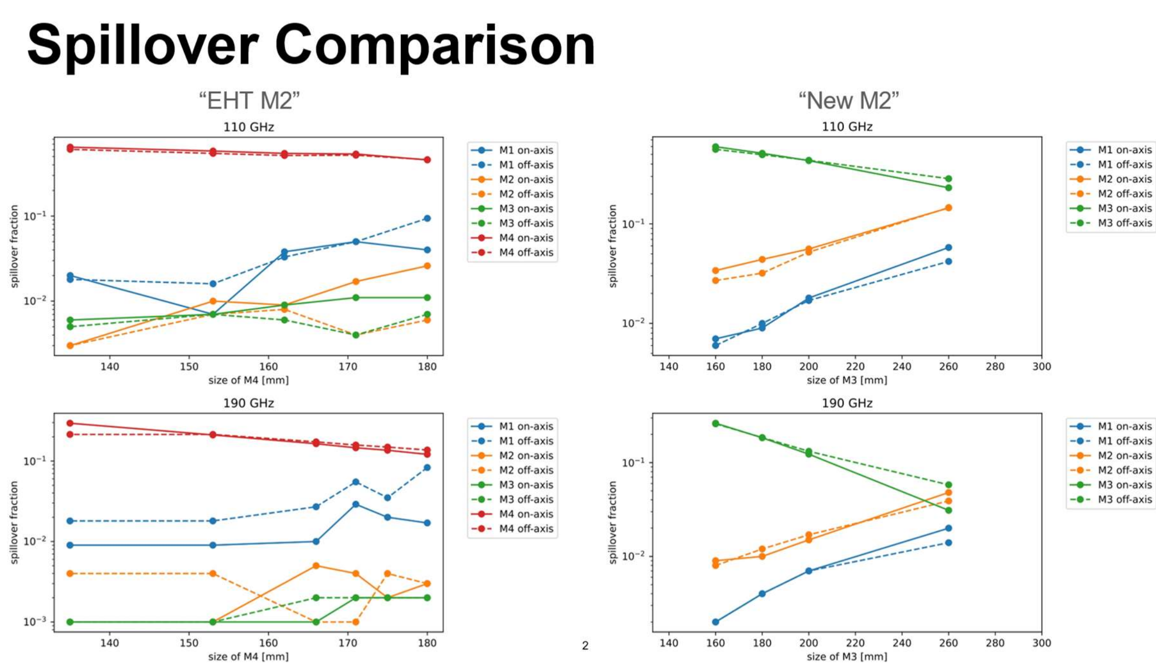

Figure 25. A comparison of spillover analysis for figure four and 3 mirror configurations

Furthermore, analysis of noise equivalent temperature (NET) for each optic was done for both configurations for three different scenarios. NET is defined as the minimum detectable temperature such that the signal from the detector through the optics is equal to its noise. [28] The lower the NET value, the better the system performance is. The results are displayed in Figures 26 through 28. The plots further confirm that, between the 180- and 200-mm range for M3, performance is on par or in some instances better than the figure four design. Results of this analysis determined that the new 3-mirror design has similar spillover and sensitivity levels to the previous figure four design. It was established that a mirror of 180 mm is roughly optimal for sensitivity. Consequently, M3 now became the stop of the system.

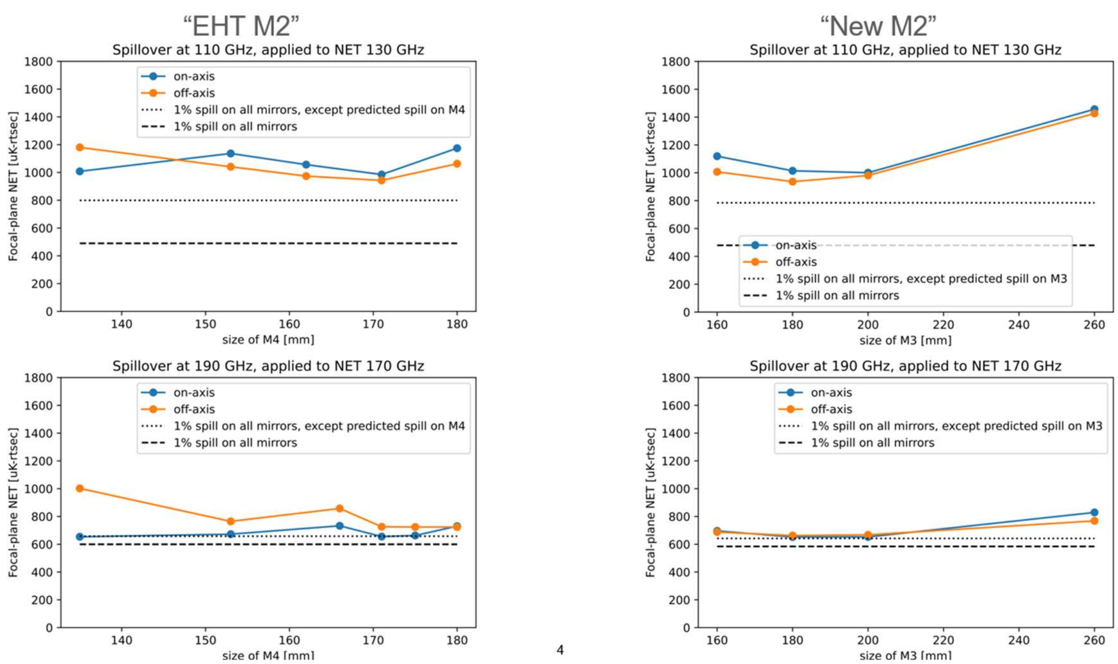

Figure 26. NET analysis for baseline configuration

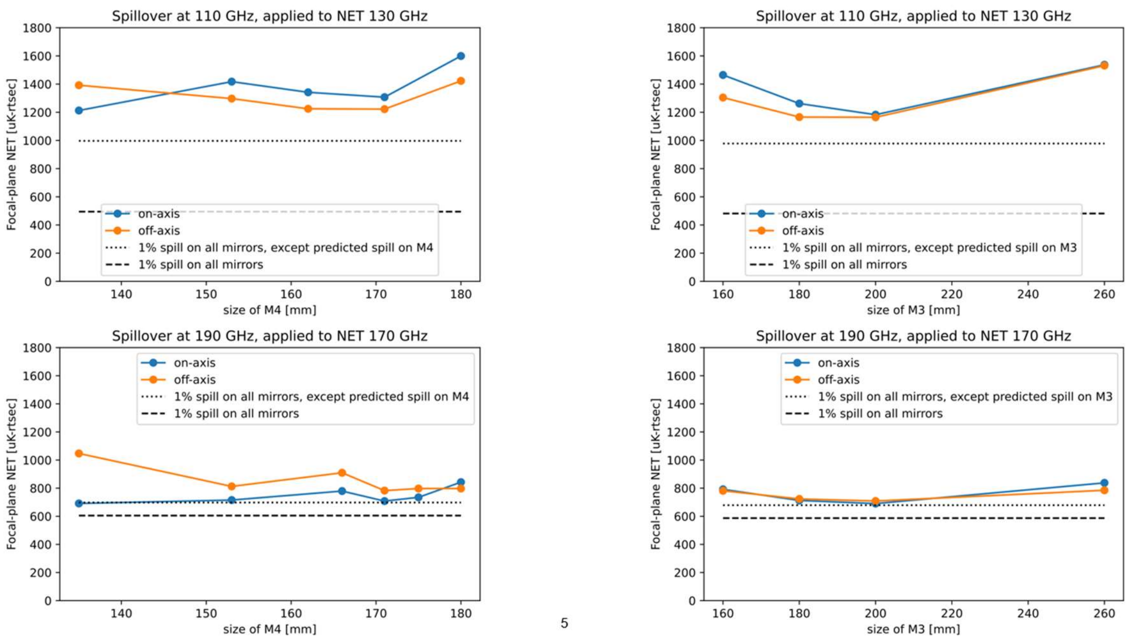

Figure 27. NET analysis for a warm folding flat

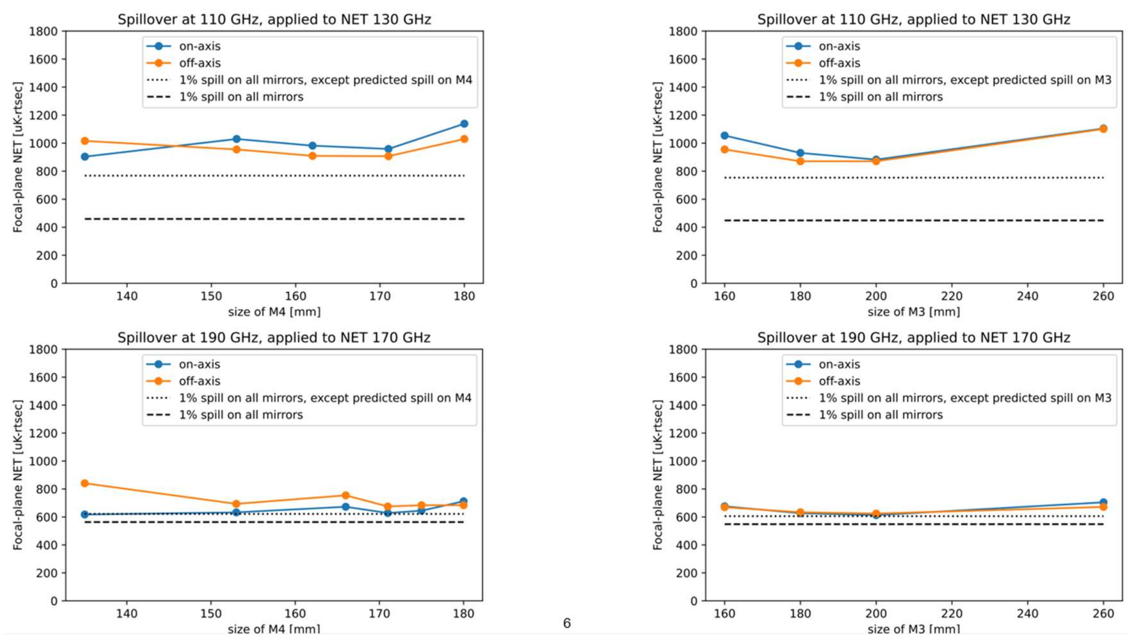

Figure 28. NET analysis for a cool primary mirror

With the design settled on an optimal size for M3, the next step was to provide an analysis on the shape of the aperture. Initially, all simulations up to this point were done with M3 modeled as a circular aperture in Zemax. A request was made to model as an elliptical aperture with 90 mm X half width and 100 Y half width. The elliptical aperture has an area of 28.27 m^2 while the circular aperture would have an area of 24.44 m^2. Theoretically, the elliptical aperture should increase the throughput of the system due to the greater area. Figure 29 shows the footprint at M3 supports this.

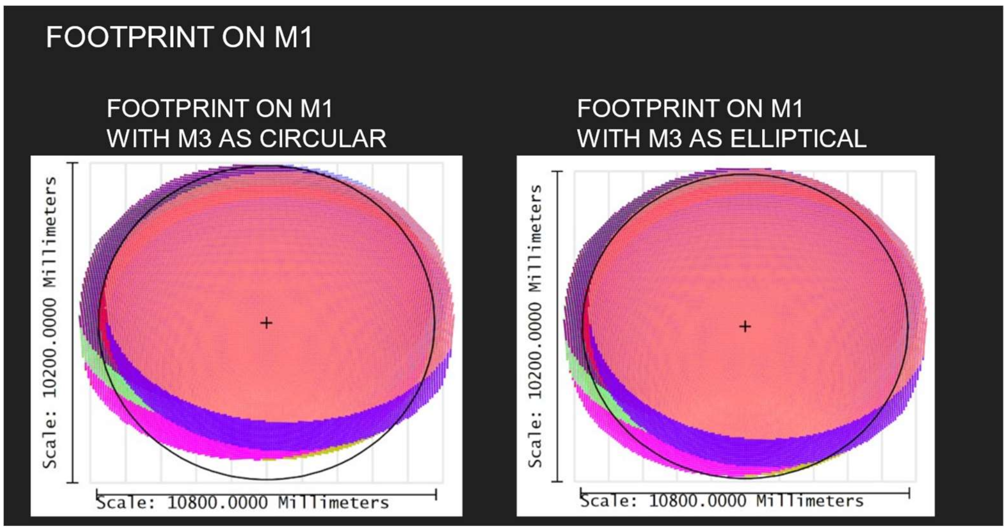

Figure 29. Beam footprint at the primary mirror. (Left) for circular M3 shape (Right) for elliptical M3 shape

The spillover analysis was rerun with the new aperture size and shape. At M1 and M2, the spillover is lower for the elliptical aperture in both the on-axis and off-axis case for both wavelengths, shown in figures 30 and 31.

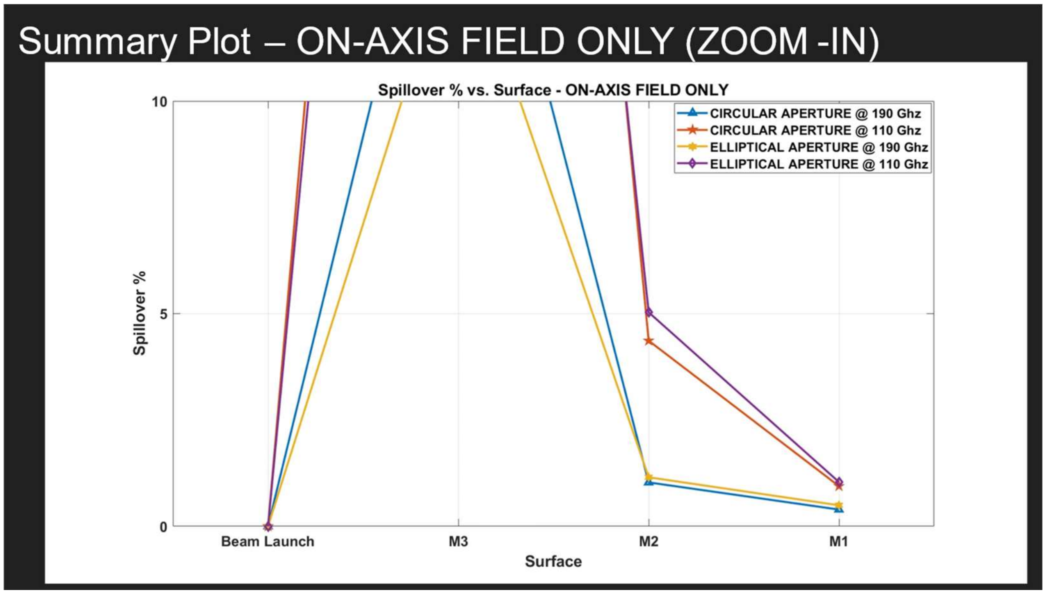

Figure 30. Spillover analysis for circular and elliptical M3 shape on-axis. Zoomed in for clarity.

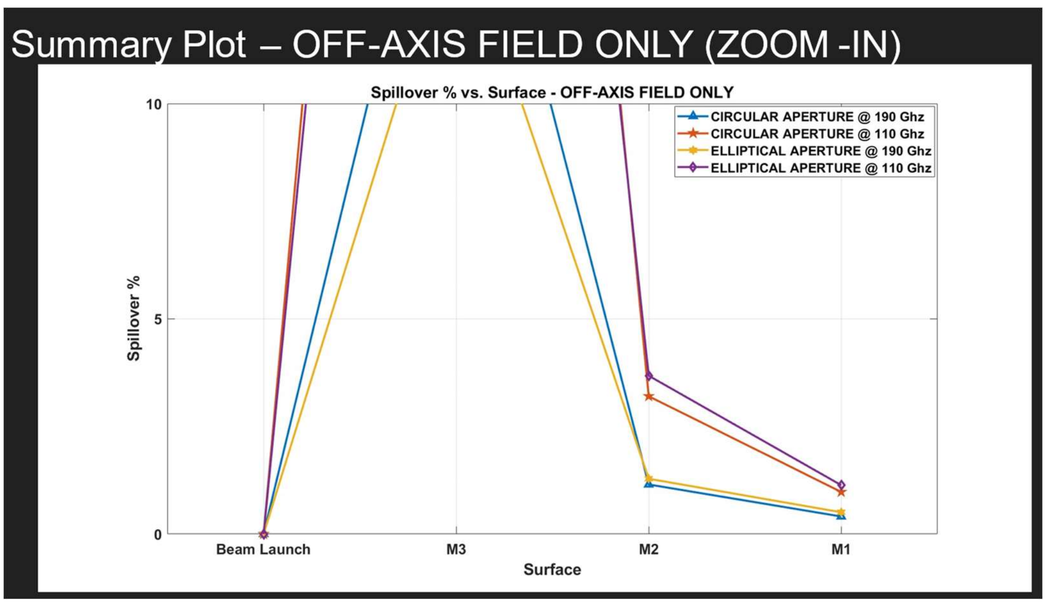

Figure 31. Spillover analysis for circular and elliptical M3 shape off-axis. Zoomed in for clarity.

The development of SPT-SLIM is an ongoing project for the next era of survey technology. Though the previous analysis marked the end of my contributions to the team at the University of Arizona, there is still a good amount of work to be done before reaching first light. The team at U of A are currently collaborating with the team at Fermilab to finalize CAD models and eventually develop drawings for the design. Once specifications in the model are agreed upon, fabrication and testing can begin, and eventually the beginning of LIM surveys.

3. Conclusion

The South Pole Telescope has been substantially contributory to our understanding of the stars. Its design has allowed it to be adaptable to several different instruments that analyze different forms of our galaxy. The 3-mirror design is simple, yet proven effective for many of its goals.

SPT-SZ was successful in detecting one of the largest galaxy clusters, known as SPT-CL J2106-5844. Some clusters were the first to be imaged altogether by the telescope. The first season data of SPTpol campaign led to the first detection of B mode polarization from gravitation lensing. Gravitational lensing is when a massive body causes spacetime to curve, and the light that travels around it is visibly bent. B modes can provide evidence of the scale of inflation after the big bang, as well as evidence of gravitational waves. The SPT-3G data continues to be analyzed today, but early datasets have been providing more constraints to ΛCDM models to make them more accurate. The success of the VLBI configuration of the SPT led to the first direct visual evidence of the M87 black hole. Not too long after, Sagittarius A*, the massive black hole at the center of our very own solar system, was imaged.

Given these accomplishments, it is no wonder why the SPT is the telescope of choice to be the pathfinder for the ever-growing field of line intensity mapping. LIM demands a wider field of view that consequently requires an upgrade in optics and receiver. Fortunately, the team at the University of Arizona has stepped up to the challenge and is currently working to finish analysis of their design, to move on to the next stage of fabrication.

References

[1] S. Chang and A. Prata, “Geometrical theory of aberrations near the axis in classical off-axis reflecting telescopes,” J. Opt. Soc. Am. A, vol. 22, no. 11, pp. 2454–2464, Nov. 2005, doi: 10.1364/JOSAA.22.002454.

[2] S. Chang, “Off-axis reflecting telescope with axially-symmetric optical property and its applications,” in Space Telescopes and Instrumentation I: Optical, Infrared, and Millimeter, J. C. Mather, H. A. MacEwen, and M. W. M. de Graauw, Eds., SPIE, 2006, p. 626548. doi: 10.1117/12.672695.

[3] “Cosmic Microwave Background | Center for Astrophysics,” www.cfa.harvard.edu. https://www.cfa.harvard.edu/research/topic/cosmic-microwave-background (accessed Apr. 08, 2024).

[4] “ESA Science & Technology - Hunting Galaxy Clusters with Planck – The Sunyaev-Zel’dovich Effect,” https://sci.esa.int/web/planck/-/48227-hunting-galaxy-clusters-with-planck-the-sz-effect, Sep. 01, 2019. https://sci.esa.int/web/planck/-/48227-hunting-galaxy-clusters-with-planck-the-sz-effect (accessed Apr. 11, 2024).

[5] J. E. Carlstrom et al., “The 10 Meter South Pole Telescope,” Publications of the Astronomical Society of the Pacific, vol. 123, no. 903, p. 568, Apr. 2011, doi: 10.1086/659879.

[6] J. Ruhl et al., “The South Pole Telescope,” in SPIE Proceedings, J. Zmuidzinas, W. S. Holland, and S. Withington, Eds., SPIE, Oct. 2004. doi: 10.1117/12.552473.

[7] J. E. Austermann et al., “SPTpol: an instrument for CMB polarization measurements with the South Pole Telescope,” in Millimeter, Submillimeter, and Far-Infrared Detectors and Instrumentation for Astronomy VI, W. S. Holland, Ed., SPIE, Sep. 2012. doi: 10.1117/12.927286.

[8] Robert Allen Meyers, Encyclopedia of physical science and technology, 3rd ed. San Diego: Academic Press, Cop, 2001.

[9] E. M. George et al., “Performance and on-sky optical characterization of the SPTpol instrument,” in Millimeter, Submillimeter, and Far-Infrared Detectors and Instrumentation for Astronomy VI, W. S. Holland, Ed., SPIE, 2012, p. 84521F. doi: 10.1117/12.925586.

[10] J. A. Sobrin et al., “The Design and Integrated Performance of SPT-3G,” The Astrophysical Journal Supplement Series, vol. 258, no. 2, p. 42, Feb. 2022, doi: 10.3847/1538-4365/ac374f.

[11] B. A. Benson et al., “SPT-3G: a next-generation cosmic microwave background polarization experiment on the South Pole telescope,” in Millimeter, Submillimeter, and Far-Infrared Detectors and Instrumentation for Astronomy VII, W. S. Holland and J. Zmuidzinas, Eds., SPIE, 2014, p. 91531P. doi: 10.1117/12.2057305.

[12] “MIRI Coronagraphs - JWST User Documentation,” https://jwst-docs.stsci.edu/jwst-mid-infrared-instrument/miri-instrumentation/miri-coronagraphs#MIRICoronagraphs-ref, Jan. 02, 2017. https://jwst-docs.stsci.edu/jwst-mid-infrared-instrument/miri-instrumentation/miri-coronagraphs#MIRICoronagraphs-ref (accessed Apr. 12, 2024).

[13] J. A. Sobrin et al., “Design and characterization of the SPT-3G receiver,” in Millimeter, Submillimeter, and Far-Infrared Detectors and Instrumentation for Astronomy IX, J. Zmuidzinas and J.-R. Gao, Eds., SPIE, 2018, p. 107081H. doi: 10.1117/12.2314366.

[14] C. Atkins, “Event Horizon Telescope (EHT) | Center for Astrophysics,” pweb.cfa.harvard.edu. https://pweb.cfa.harvard.edu/facilities-technology/telescopes-instruments/event-horizon-telescope-eht (accessed Apr. 08, 2024).

[15] R. T. Schilizzi, “Very long baseline interferometry,” Radio Science, vol. 21, no. 4, pp. 665–679, 1986, doi: https://doi.org/10.1029/RS021i004p00665.

[16] J. Kim et al., “A VLBI receiving system for the South Pole Telescope,” in Millimeter, Submillimeter, and Far-Infrared Detectors and Instrumentation for Astronomy IX, J. Zmuidzinas and J.-R. Gao, Eds., SPIE, 2018, p. 107082S. doi: 10.1117/12.2301005.

[17] T. J. Brendel, “Optical Solutions to Telescope Problems: Stray Light Analysis, Laser-Truss Metrology, and Freeform Optical Design.” The University of Arizona., 2023. [Online]. Available: http://hdl.handle.net/10150/668304

[18] T. Oxholm, “A Beginner’s Guide to Line Intensity Mapping Power Spectra,” Proceedings of the Wisconsin Space Conference, Feb. 2022, doi: 10.17307/wsc.v1i1.352.

[19] E. D. Kovetz et al., “Astrophysics and Cosmology with Line-Intensity Mapping.” 2019.

[20] J. L. Bernal and E. D. Kovetz, “Line-intensity mapping: theory review with a focus on star-formation lines,” The Astronomy and Astrophysics Review, vol. 30, no. 1, Sep. 2022, doi: 10.1007/s00159-022-00143-0.

[21] K. S. Karkare et al., “SPT-SLIM: A Line Intensity Mapping Pathfinder for the South Pole Telescope,” Journal of Low Temperature Physics, vol. 209, no. 5–6, pp. 758–765, Mar. 2022, doi: 10.1007/s10909-022-02702-2.

[22] K. Garrard, T. Bruegge, J. Hoffman, T. Dow, and A. Sohn, “Design tools for freeform optics,” in Current Developments in Lens Design and Optical Engineering VI, P. Z. Mouroulis, W. J. Smith, and R. B. Johnson, Eds., SPIE, 2005, p. 58740A. doi: 10.1117/12.617680.

[23] I. Trumper, A. Q. Anderson, J. M. Howard, G. West, and D. W. Kim, “Design form classification of two-mirror unobstructed freeform telescopes,” Optical Engineering, vol. 59, no. 2, p. 025105, 2020, doi: 10.1117/1.OE.59.2.025105.

[24] A. Locke, “Exploring Physical Optics Propagation (POP) in OpticStudio,” Mar. 31, 2021. https://support.zemax.com/hc/en-us/articles/1500005488421-Exploring-Physical-Optics-Propagation-POP-in-OpticStudio (accessed Apr. 08, 2024).

[25] A. SPT, “SPT-SLIM Electronics Rack and Detector Forecasting”.

[26] W. Park et al., “Flight model characterization of the wide-field off-axis telescope for the MATS satellite,” Applied Optics, vol. 59, no. 17, p. 5335, Jun. 2020, doi: 10.1364/ao.392187.

[27] D. Hill, “What is Polynomial Sensitivity Tolerancing?,” Mar. 31, 2021. https://support.zemax.com/hc/en-us/articles/1500005488401-What-is-Polynomial-Sensitivity-Tolerancing (accessed Apr. 08, 2024).

[28] www.lasercomponents.com. “LASER COMPONENTS Germany,” February 2019. https://www.lasercomponents.com/de/?embedded=1&file=fileadmin/user_upload/home/Datasheets/lc/application-reports/lc-pyros/calculation-net.pdf&no_cache=1.